Supplementary information for deep subsurface water can sustain giant sequoias

Benjamin J. Eppinger[1], W. Steven Holbrook[1], Dario Grana [2], Clifford S. Riebe [2], Claire E. Lukens [3], Antony R. Ambrose[4], Sean P. Bemis[1], Denise Burgett[1], Anya R. Gupta[1], Shiv M. Gupta[1]

[1]Department of Geosciences, Virginia Polytechnic Institute and State University, Blacksburg, VA, USA

[2]Department of Geology and Geophysics, University of Wyoming, Laramie, WY, USA

[3]Department of Life and Environmental Sciences and Sierra Nevada Research Institute, University of California Merced, Merced, California, USA

[4]Ancient Forest Society, South Lake Tahoe, CA, USA

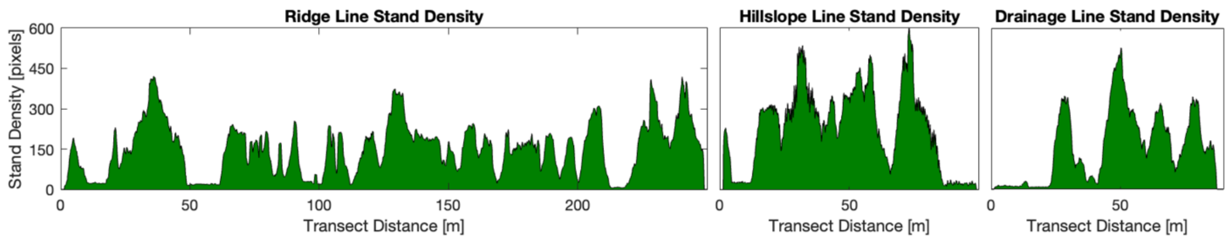

Figure S1: Stand density estimates using the combined handheld and ariel lidar point clouds shown in Figures 2 and 3. We quantity stand density along the geophysics as a function of transect distance by summing together all the pixels that record a lidar return at each location along the transect.

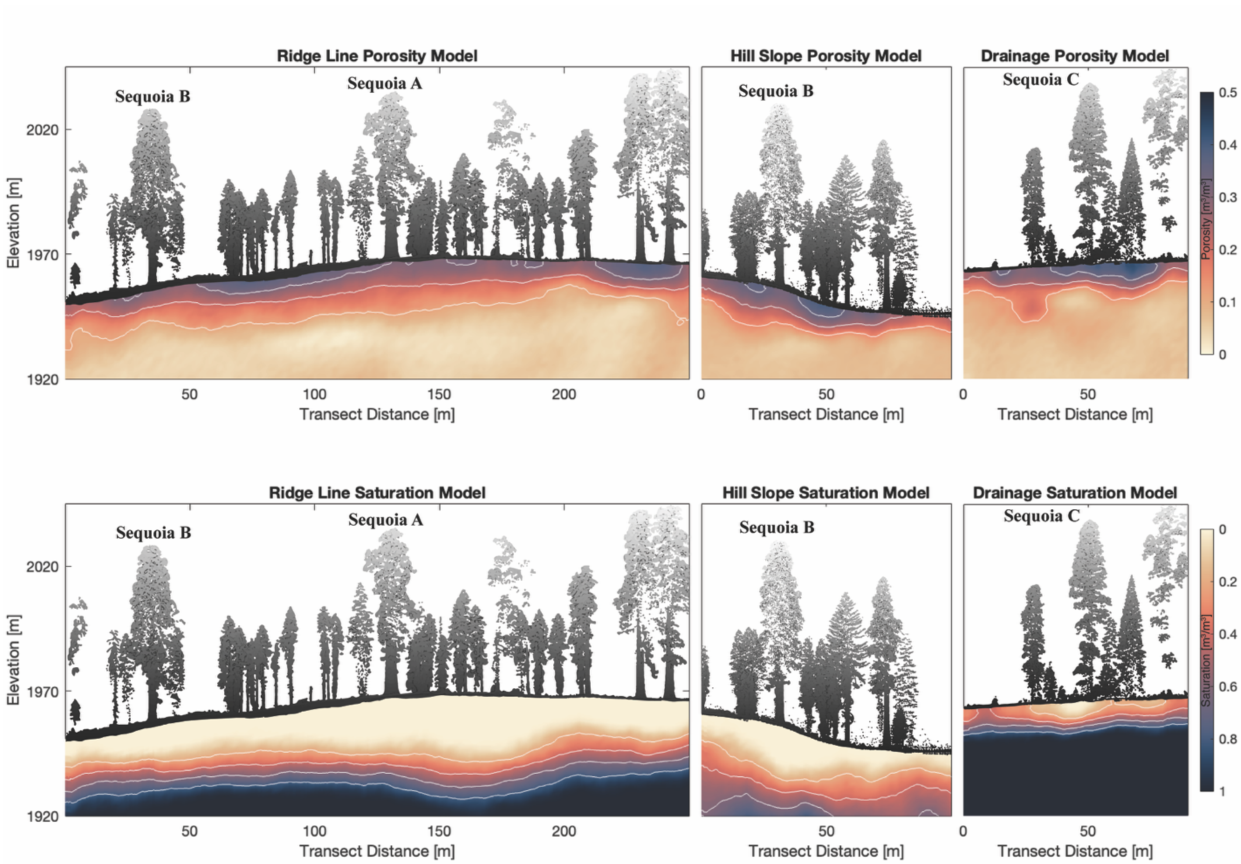

Figure S2: Geostatistical rock physics inversion results from the three different profiles demarcated in Figure 1. The giant sequoias labeled in Figure 1 are also labeled in this figure.

The top row shows porosity models with white contours at 0.1 increments, with darker colors showing more porous material. The bottom row shows saturation models with white contours at 0.2 m/s increments, with darker colors showing more saturated material. Overlying each cross-section are vegetation point clouds derived from handheld and aerial lidar measurements.

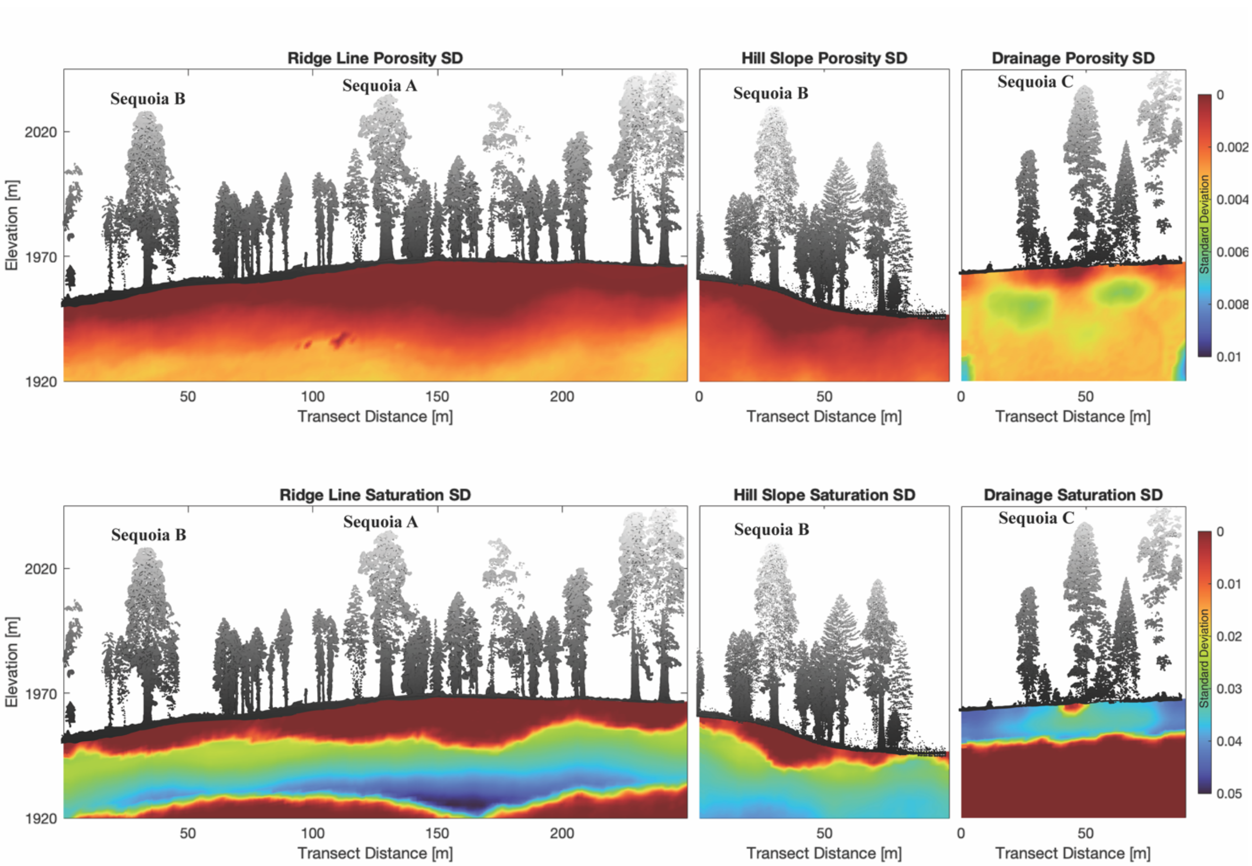

Figure S3: Geostatistical rock physics inversion results corresponding to the standard deviation of the porosity and saturation fields from the three different profiles demarcated in Figure 1. The giant sequoias labeled in Figure 1 are also labeled in this figure. The top row shows porosity standard deviation models. The bottom row shows saturation standard deviation models. Overlying each cross-section are vegetation point clouds derived from handheld and aerial lidar measurements.

Seismic Inversion

In general, seismic inversion methods are designed to constrain elastic velocities using waveforms recorded by geophones (sometimes also referred to as receivers). Given observed seismograms, full waveform inversion (FWI) determines the P- and S-wave velocity models that generate synthetic data matching the field recordings. This is done by iteratively minimizing the misfit between observed and simulated waveforms using numerical solutions to the elastic wave equation. This method has become widely-used for high-resolution seismic imaging because it simultaneously matches multiple waveform phases contained in the seismic signal, including p-waves, s-wave, and surface waves. Here, we demonstrate the method's suitability for critical zones FWI with a synthetic test showing that FWI can recover near surface variations in Vp, Vs, and Vp:Vs ratio. Then, we validate the inversion of the Yosemite dataset by comparing synthetic seismograms from the FWI-derived velocity models with corresponding field record sections. Because the misfit functional we employ for FWI specifically minimizes windowed time lags between observed and synthetic traces, we also show histograms of all the measured time lags for each profile before and after FWI. Narrowing of the time lag distributions shows the extent to which the FWI has fit the data.

<u>Synthetic FWI Test</u>

To verify our FWI approach, we implement a synthetic test using the acquisition geometry of the Ridge Line. The Vp and Vs initial models are the same as those used for the real-data inversion. For the synthetic test, we create target models by adding velocity anomalies to the initial models. The initial models (left column of Figure S4) have a uniform Vp:Vs ratio of 2. We added velocity anomalies (top right panel of Figure S4) to the Vp initial model. We added the same velocity anomalies (bottom right panel of Figure S4) to the Vs initial model, as well as four additional anomalies in the upper 20 m. Because we added additional velocity anomalies to the Vs model, the target Vp:Vs model is not spatially homogenous. After creating the target models, we used specfem2d to simulate synthetic elastic waveform data corresponding to these models. Then starting from the initial model, we applied our FWI workflow to the synthetic data.

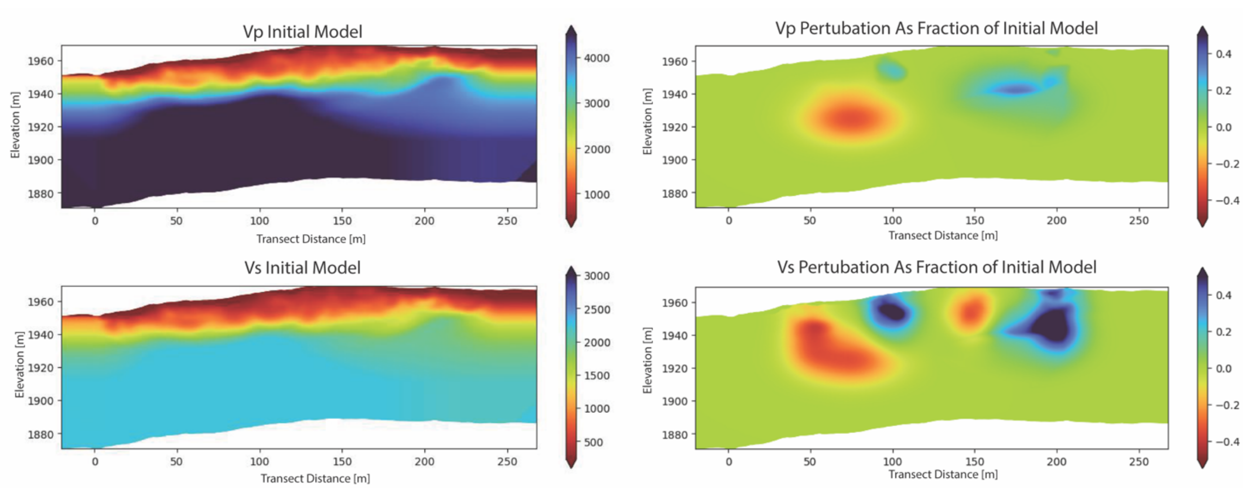

Figure S4: The left top panel shows in the initial Vp model while the bottom left shows the initial Vs model. The right top panel shows the two velocity perturbations as a fraction of the initial velocity model, or equivalently stated, the velocity perturbations divided by the initial model. The bottom panel shows the velocity perturbations for the Vs model. The velocity perturbation models in the right column are used to construct the target models from the initial models.

The results from the synthetic test show to what extent we are able to recover the target velocity models with our FWI workflow. The upper 30 m of the inverted Vp model (top right panel of Figure S5) matches the target model (top left panel of Figure S5), but the velocity anomalies are not recovered as well at greater depths. In general, the inverted Vs model (middle right panel of Figure S5) matches the target model (middle left panel of Figure S5) better than the inverted Vp model, but inaccuracies in the inverted Vs model also increase with depth. The resultant Vp:Vs ratio of the inverted models (bottom right panel of Figure S5) matches the target Vp:Vs ratio model (bottom right panel of Figure S5) well in the upper 30 m, but at greater depths, inaccuracies in the inverted Vp and Vs models manifest as artifacts in the deep parts of the Vp:Vs ratio model. Note that our analysis in the main text focuses on features in the upper 30 m of the subsurface where, from the synthetic FWI test, the velocity models appear to be well constrained.

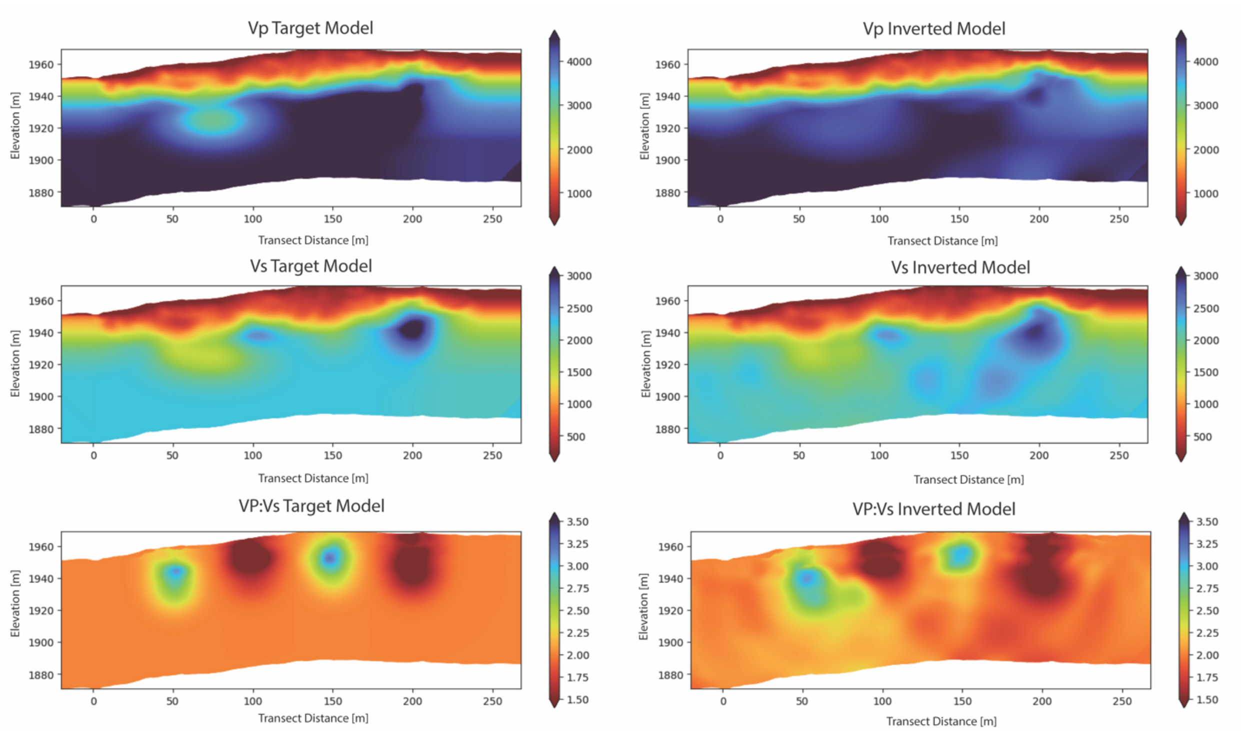

Figure S5: The left column shows the target models that we try to recover with the synthetic FWI test. The right column shows the inverted models from the synthetic FWI test. Vp models are shown in the top row, Vs model in the middle, and Vp:Vs ratio models in the bottom. The inverted Vp:Vs ratio model is computed after FWI from the inverted Vp and Vs models.

FWI Results Validation

Below, we show several sample shot gathers of preprocessed observed and synthetic data with muting, trace normalization, and 5-65 Hz bandpass filtering. The synthetic data are generated from the final FWI velocity models (inverted from the observed data). We show one representative shot gather for each component from each seismic profile. For the Ridge Line, we show both horizontal (Figure S6) and vertical component shot gathers (Figure S7). For the Hillslope and Drainage Lines, we show only vertical component shot gathers because this was the only component of seismic data collected and inverted (Figures S8 and S9 respectively). The shot gathers provide a means to qualitatively benchmark the FWI. In the additional data files, we have also included trace by trace comparisons of observed and modelled data for all shots across and profiles. We note that, in general, the phase velocities of the observed and synthetic data tend to match well, implying that the FWI of the field data was successful. We also show histograms of all the measured time lags for each profile before and after FWI (Figures S10-S12).

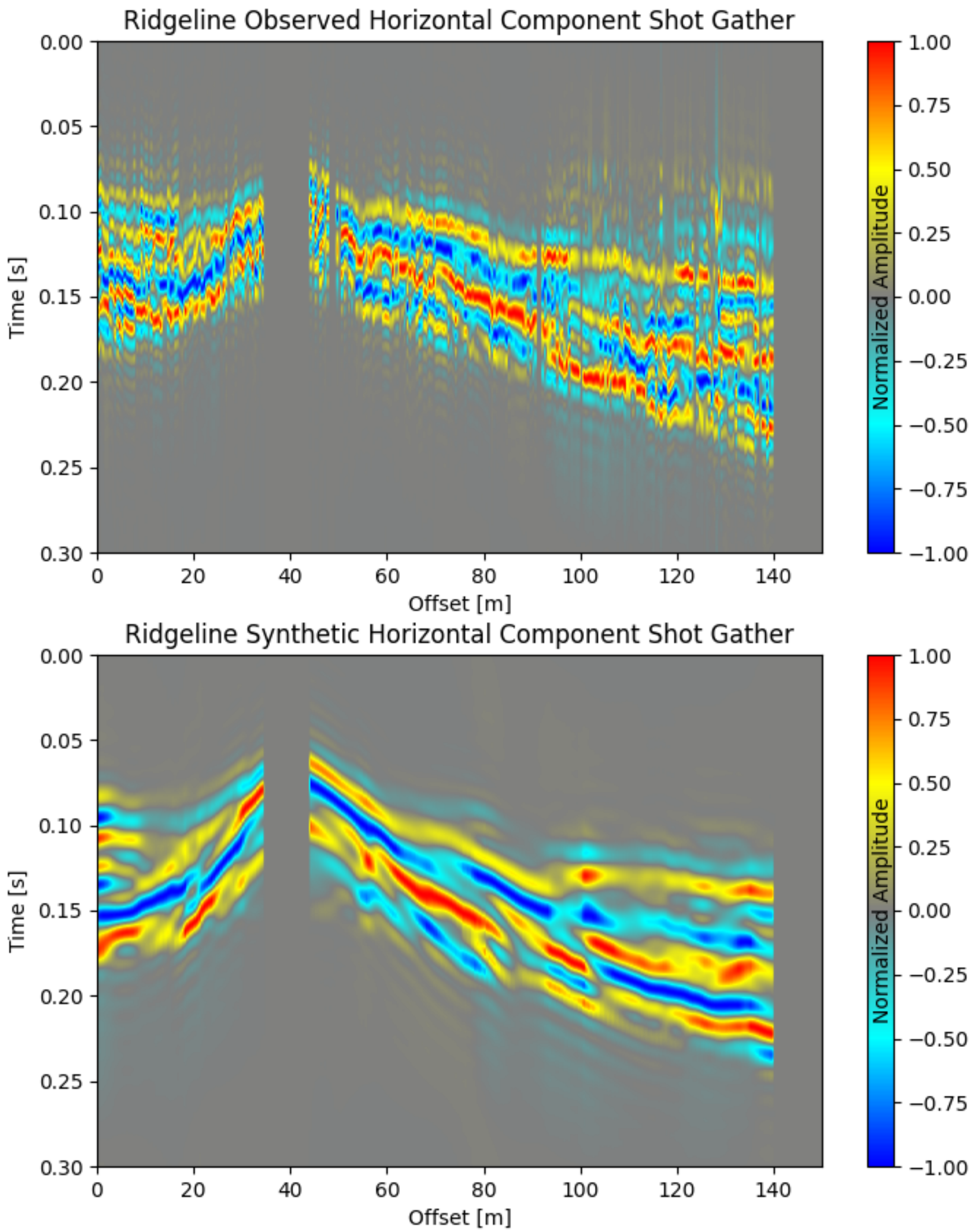

Figure S6: (Top) A horizontal component shot gather from the ridge line. The data were collected on a 250-m-long linear array of autonomous nodal instruments spaced at 0.5 m intervals. The data has been preprocessed with slope muting, offset muting, trace normalization, and 5-65 Hz bandpass filtering. (Bottom) The corresponding synthetic horizontal component shot gather modeled using the final ridgeline FWI model, processed with the same preprocessing steps.

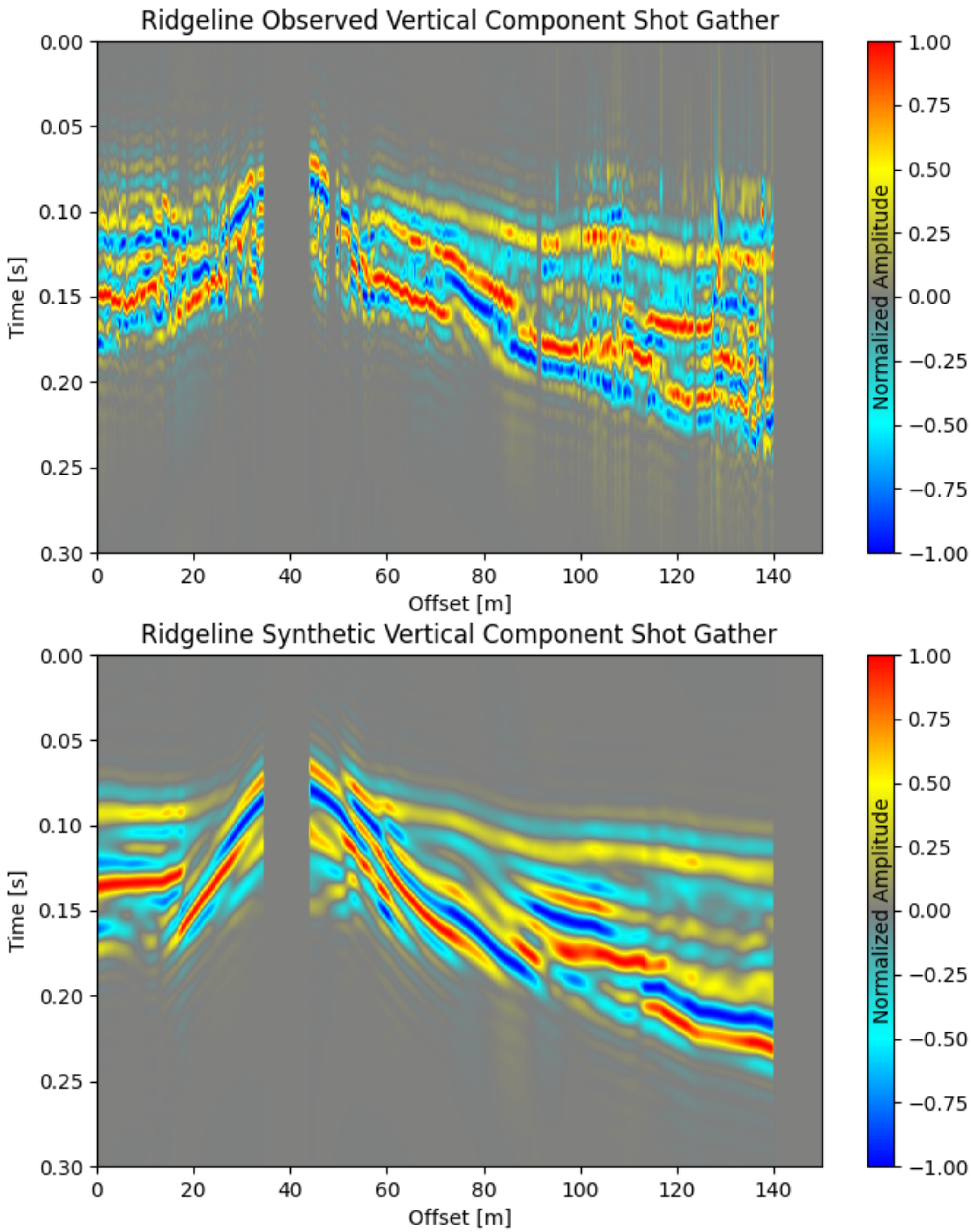

Figure S7: (Top) A vertical component shot gather from the ridge line. The data were collected on a 250-m-long linear array of autonomous nodal instruments spaced at 0.5 m intervals. The data have been preprocessed with slope muting, offset muting, trace normalization, and 5-65

Hz bandpass filtering. (Bottom) The corresponding synthetic vertical component shot gather modeled using the final ridgeline FWI model, with the same preprocessing steps applied.

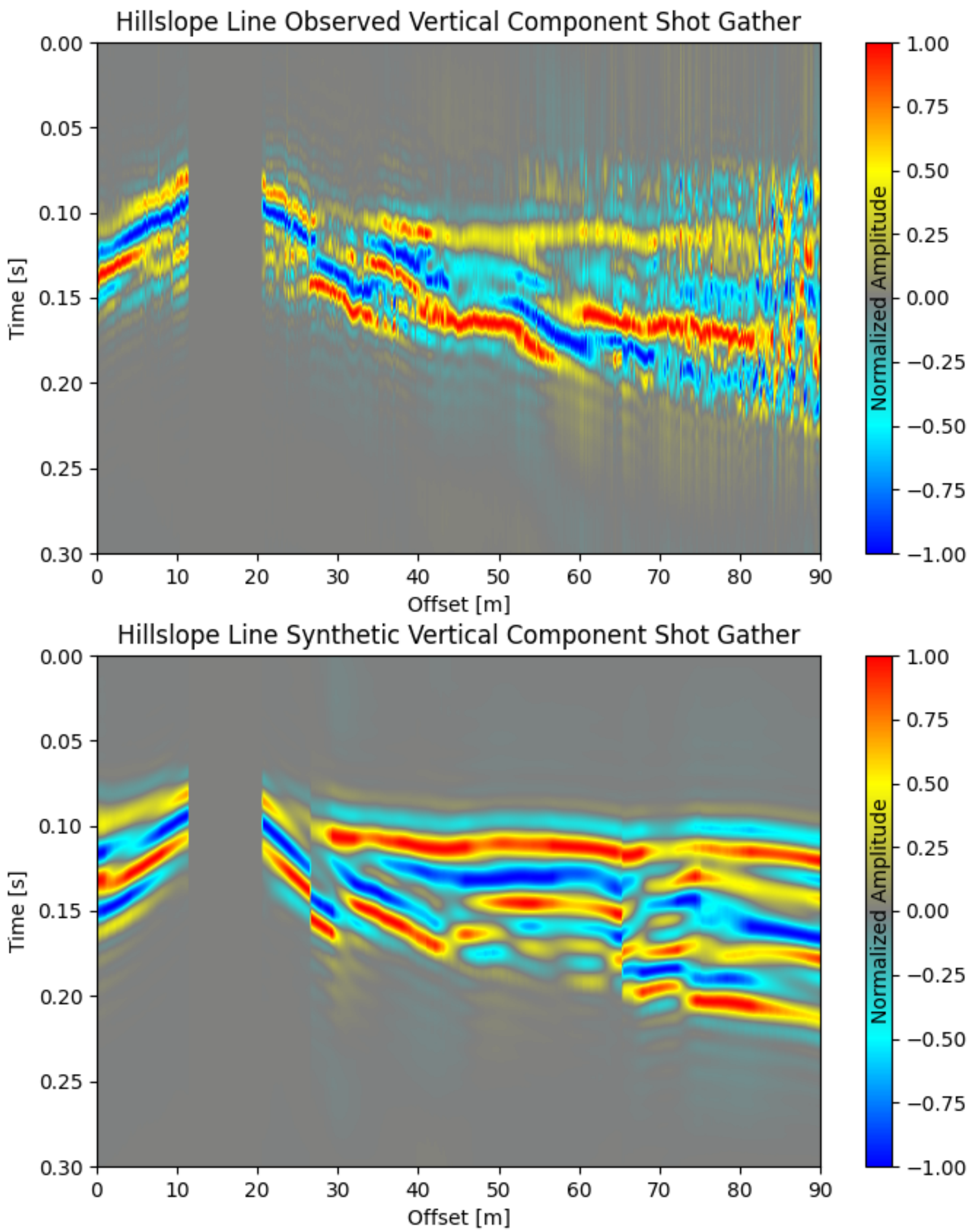

Figure S8: (Top) A vertical component shot gather from the hillslope Line. The data were collected on a 90-m-long linear array of autonomous nodal instruments, spaced at 0.2 m intervals. The data has been preprocessed with slope muting, offset muting, trace normalization, and 5-65 Hz bandpass filtering. (Bottom) The corresponding synthetic vertical component shot gather modeled using the final Hillslope Line FWI model. The same preprocessing steps have been applied to the synthetic shot gather.

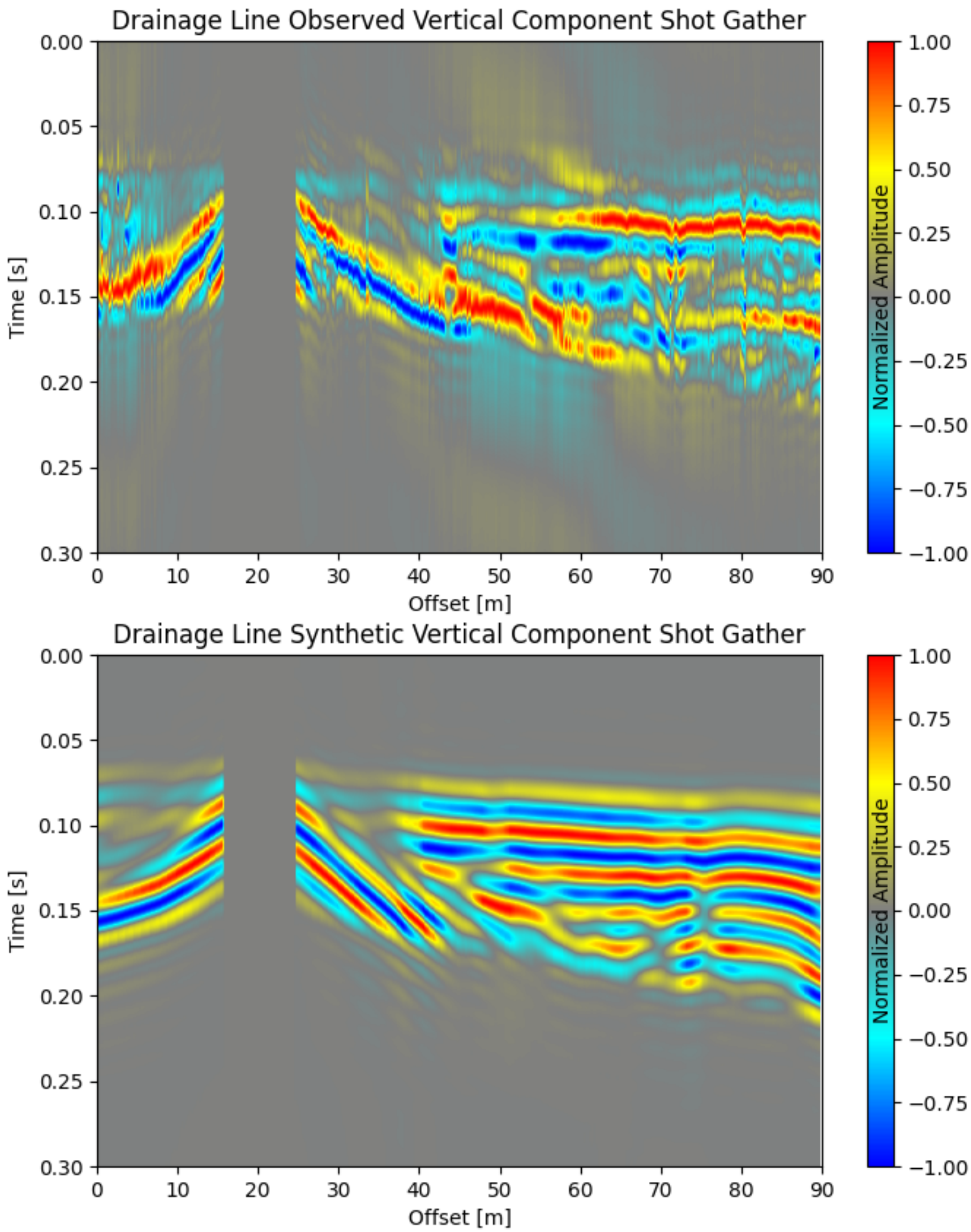

Figure S9: (Top) A vertical component shot gather from the drainage line. The data were collected on a 90-m-long linear array of autonomous nodal instruments spaced at 0.25 m intervals. The data have been preprocessed with slope muting, offset muting, trace normalization, and 5-65 Hz bandpass filtering. (Bottom) The corresponding synthetic vertical component shot gather modeled using the final Drainage Line FWI model. Note that the same preprocessing steps have been applied to the synthetic shot gather.

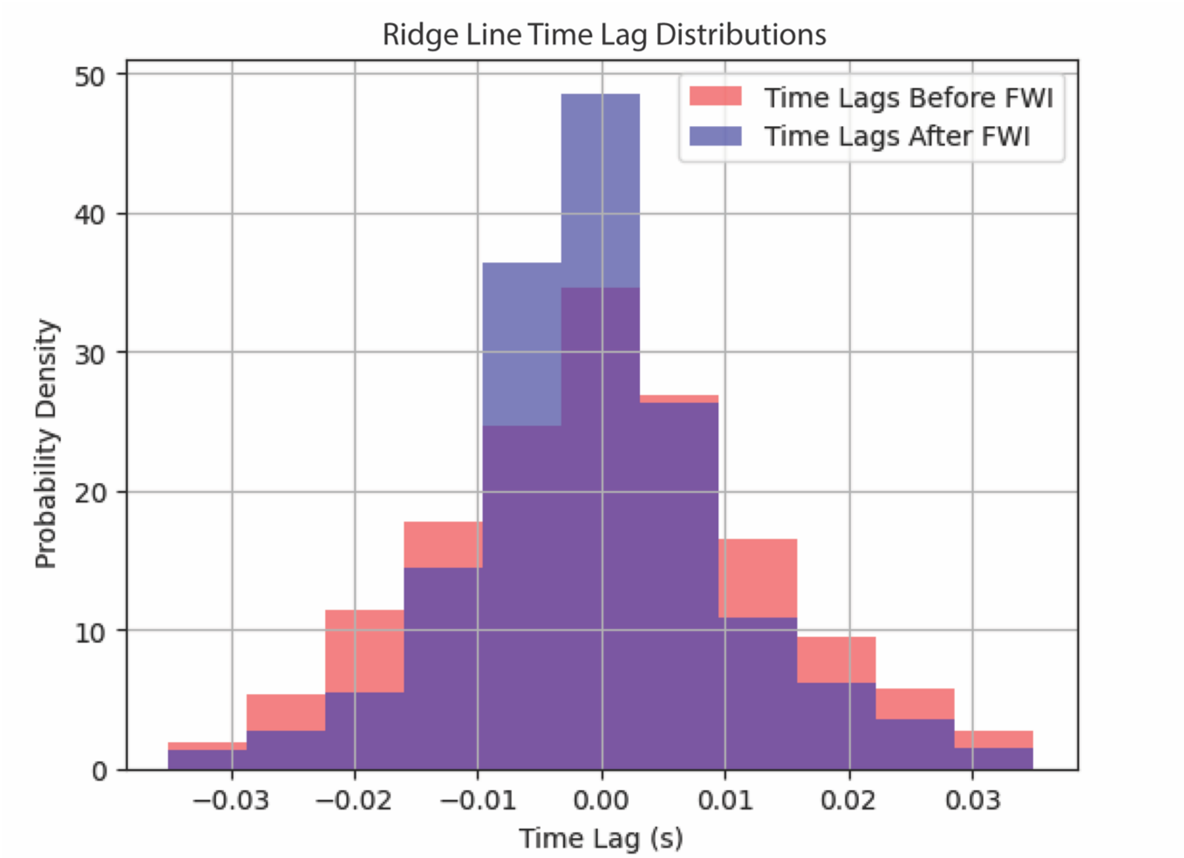

Figure S10: Time lag distributions calculated from the ridge line model before and after FWI. The lags from before are shown in red and after are shown in blue. The red and blue histograms are both plotted with 50 % transparency, so where they overlap appears as purple.

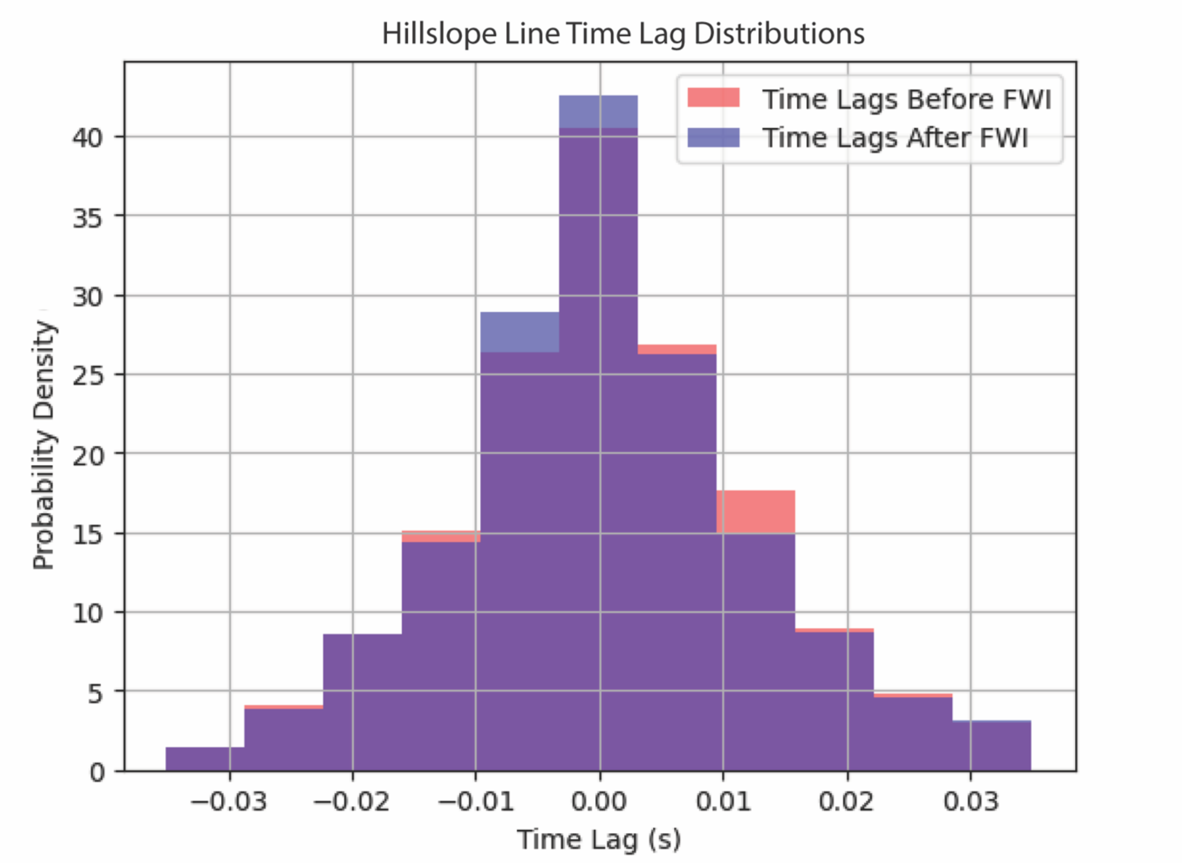

Figure S11: Time lag distributions calculated from the hillslope line model before and after FWI. The lags from before are shown in red and after are shown in blue. The red and blue histograms are both plotted with 50 % transparency, so where they overlap appears as purple.

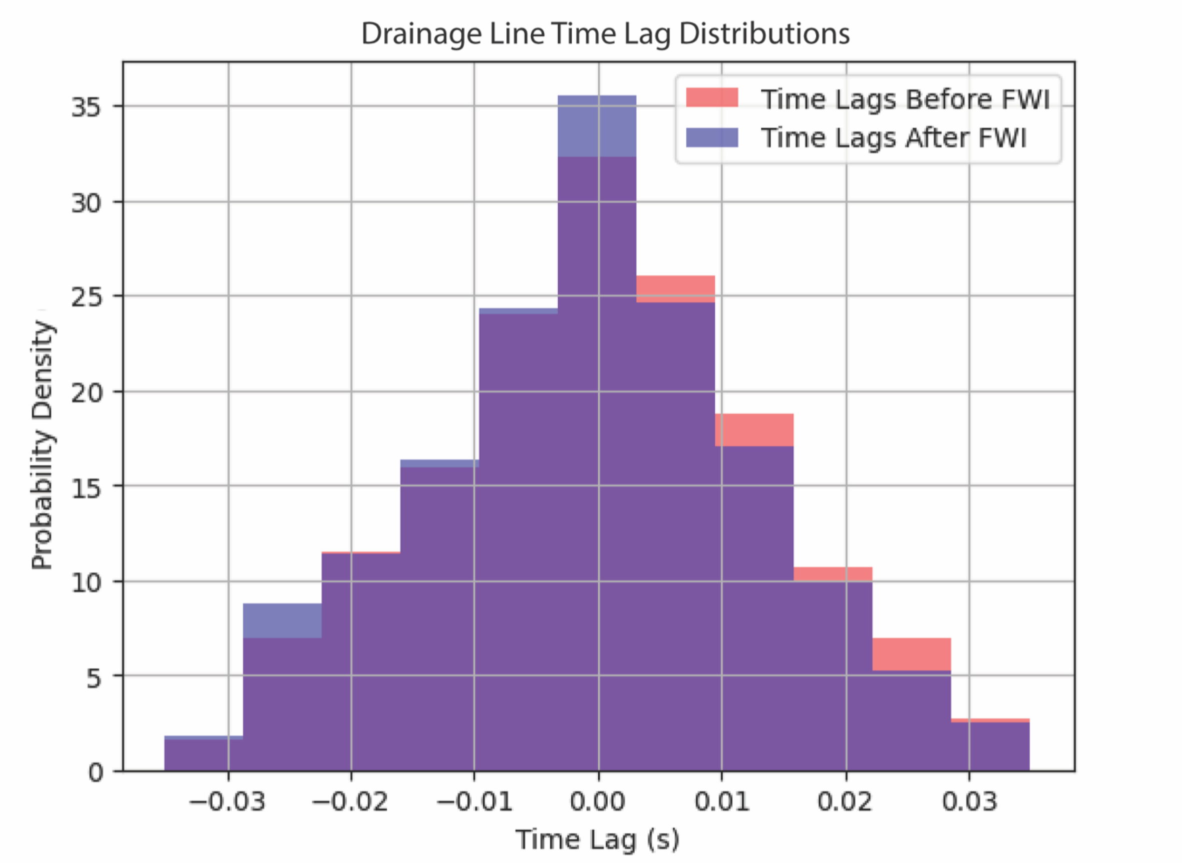

Figure S12: Time lag distributions calculated from the drainage line model before and after FWI. The lags from before are shown in red and after are shown in blue. The red and blue histograms are both plotted with 50 % transparency, so where they overlap appears as purple.

Profile	Date Collected	Vertical Component	Horizontal Component	Geophone Spacing	Source Spacing
Ridge Line	1 Aug 2023	Yes	Yes	0.5 m	5 m
Hillslope Line	22 Jul 2024	Yes	No	0.2 m	1 m
Drainage Line	25 Jul 2023	Yes	No	0.25 m	2 m

Table S1: acquisition parameters for seismic surveys.

Sample	Water Content (g/g)	Average	Standard Deviation
Sequoia A I (Ridge)	0.033	0.054	0.019
Sequoia A II (Ridge)	0.092		
Sequoia A III (Ridge)	0.036		
Sequoia B I (Hillslope)	0.075	0.057	0.018
Sequoia B I (Hillslope)	0.038		
Sequoia C I (Drainage)	0.135	0.128	0.016
Sequoia C II (Drainage)	0.098		
Sequoia C III (Drainage)	0.151		

Table S2: Soil moisture measurements around giant sequoias during August of 2025.